Volume 15, Issue 1, 152510 (1-13)

Iranian Journal of Catalysis (IJC)

https://doi.org/10.57647/j.ijc.2025.1501.10

Optimization of photocatalytic degradation of safranin O under UV and visible light using $ZnFe_2O_4$ coated graphited sand in batch and continuous systems

Hussein A. Khalaf*, Mariam Essam, Emad A. Matter, G. Esmail

Chemistry Department, Faculty of Science, Damanhour University, Damanhour, Egypt.

***Corresponding author:** hkhalaf70@sci.dmu.edu.eg

Original Research

Received:
24 October 2024
Revised:
27 December 2024
Accepted:
23 January 2025
Published online:
27 January 2025

Abstract:

Zinc ferrite (ZF) coated graphited sand (GS) was synthesized using the coprecipitation method. The produced zinc ferrite-coated graphitic sand (ZFGS) has been characterized by X-ray diffraction (XRD), Scan Electron Microscopy (SEM), Energy-dispersive X-ray Spectroscopy (EDS), Brunauer-Emmett-Teller (BET), Fourier Transform Infrared Spectroscopy (FTIR), Diffuse Reflectance Spectroscopy (DRS), and zeta potential measurements. The ZFGS catalyst was employed for the photodegradation of safranin O under both UV and visible light. Photodegradation experiments were conducted using batch and fixed-bed column methods under varying conditions. A fractional factorial design was utilized to assess the effects of pH, dye concentration, irradiation time, and catalyst dosage on degradation efficiency, with interactions analyzed through Analysis of Variance (ANOVA). The ANOVA results indicated that pH, catalyst dosage, and irradiation time significantly influenced degradation, while dye concentration had minimal impact. Optimization showed a strong agreement between experimental and predicted degradation efficiencies, supported by a high correlation coefficient and significant F-ratio, validating the model. Maximum degradation efficiencies of 98.8% under UV light and 90.4% under visible light were achieved at optimal conditions: 50 mg/L dye concentration, 0.3 g catalyst dosage, pH 9, and 45 minutes of irradiation. Breakthrough curve analysis highlighted strong interactions among these variables.

Keywords: Coated sand; Fixed-bed column; Factorial study; Photocatalysis; Safranin O; Zinc ferrite

1. Introduction

Synthetic dyes have extensive applications across various sectors, including textile, leather, paper, printing, paint, pigments, cosmetics, rubber, plastic, pesticide, and pharmaceutical industries. Over 15% of synthetic dyes are lost in the wastewater stream during production and processing [1]. The contamination of water bodies by synthetic dyes from various industrial processes poses a significant environmental challenge due to their persistence and potential toxicity. In response to this issue, a variety of chemical and physical treatment methods have been developed, such as precipitation, adsorption, air stripping, flocculation, reverse osmosis, and ultrafiltration [2–4]. However, these methods are not cost-effective as they simply transfer non-biodegradable substances into sludge, creating new issues that require further treatment. In contrast, advanced oxidation processes (AOPs) offer a superior alternative for eliminating dyes and various persistent organic pollutants from wastewater [5–7]. AOPs, such as photocatalytic oxidation, Fenton reactions, electrochemical oxidation reactions, sonochemical oxidation, and others, can completely degrade organic pollutants by producing extremely reactive radicals [8, 9]. Photocatalysis has emerged as an efficient method for the degradation of pollutants. Photocatalytic degradation has gained attention as a cost-effective and efficient method for the removal of dye pollutants from wastewater. Photocatalysis theory relies on the redox properties of photocatalysts under light exposure. Typically, semiconductors serve as catalysts in photocatalytic reactions to degrade organic pollutants into CO_2 and H_2O. A semiconductor photocatalyst comprises valence band (VB) and conduction band (CB) structures, with the forbidden band existing between them. When the semiconductor catalyst absorbs photons of specific energy, it produces electrons and holes (e^- and h^+) with reduction

and oxidation capabilities, respectively [10–12]. The recombination of photogenerated e^-/h^+ pairs can significantly decrease the efficiency of the photodegradation process. Therefore, decreasing the (e^-/h^+) recombination in photocatalytic materials is vital for enhancing their efficiency, as recombination reduces the availability of charge carriers needed for photocatalytic reactions. Rezaei et al. explain various strategies used to minimize e^-/h^+ recombination [13].

In the literature, several high-quality semiconductors have been studied for their photocatalytic capabilities, particularly transition metal oxides. Among these, zinc oxide stands out for its exceptional performance. Zinc oxide (ZnO) is an n-type semiconductor with a direct bandgap of approximately 3.2 eV [14, 15] and eco-friendly properties, making it suitable for large-scale production. While ZnO can be activated by UV light, its efficiency diminishes in the visible range of sunlight due to its wide bandgap. To modify the photoactivity of ZnO, it has been modified with various materials like graphene, cellulose acetate, conducting polymer, spinel ferrite, carbon-doped materials, CuO, WO_3, and others [16–19]. Fe_2O_3 is recognized as an eco-friendly, thermally stable, and effective photocatalyst with a bandgap of approximately 2.2 eV. This photocatalyst is activated by the visible part of the solar energy spectrum and has demonstrated significant efficacy in dye degradation [14].

Safranin O (SO), also known as basic red 2, is a versatile and widely used biological dye with a rich history and a range of applications across various fields, including food coloring additives, dying for silk, wool, and cotton, and in manufacturing of paints and printing inks. The observed efficiency of photodegradation of SO dye in the presence of ZnS nanoparticles was found to be 51%. El-Kemary et al. reported that the maximum observed degradation efficiency of SO is about 60% for TiO_2 and 96% for Ag-TiO_2 [1]. Recent studies have focused on creating core/shell nanoparticles, which have garnered interest for their enhanced properties. Metal oxides like TiO_2, Fe_2O_3, and ZnO can be used separately or with modification by other dopenants for advanced photocatalytic pollutant degradation [20–22]. Sand is gaining attention for its applications in catalysis as a supporting material due to its high surface area and low cost. Heterogeneous photoreactors, for the photodegradation of pollutants, utilize photocatalysts in suspended or immobilized forms. Slurry photocatalysis drawbacks include challenges in separating or filtering the photocatalyst post-process, particle aggregation at high concentrations, and limitations in continuous processes [23–25]. To address these issues, immobilized photocatalysts are recommended, with options including glass, silica, polymers, and clays as support materials.

Factorial design is used to achieve optimal overall process optimization [26]. This experimental design allows for the determination of the effect of each factor on the response, as well as how the effect of each factor changes with varying levels of the other factors. Interaction effects between different factors can only be identified using an experimental design [27]. Compared to one-factor-at-a-time experiments, factorial designs are more efficient and enable the detection of interactions [28]. This technique helps reduce the number of experiments, time, and overall process cost while still achieving better responses. Fewer studies have explored the photodegradation of SO dye under UV and visible light using a continuous model.

In this study, a new composite material, zinc ferrite-coated graphited sand, was synthesized by coating graphite-coated sand with zinc ferrite, providing a unique catalyst for photocatalytic degradation applications under both UV and visible light. The composite ZFGS was employed for the photodegradation of safranin O dye under both UV and visible light. A fractional factorial design and ANOVA were applied to analyze the effects of key variables (pH, dye concentration, irradiation time, and catalyst dosage) on dye degradation efficiency. This statistical approach validated the model with strong predictive power, enabling optimization of operational conditions for maximum photodegradation performance. Moreover, the photodegradation process of SO dye was studied using batch and fixed bed column study.

2. Materials and methods

2.1 Materials

The following materials were utilized during the synthesis and photocatalytic measurements; Iron chloride hexahydrates ($FeCl_3.6H_2O$,97%), Zinc chloride ($ZnCl_2$, $\geq$ 98%), Nitric acid (HNO_3, 65%), Hydrochloric acid (HCl, 36%), Ethylene glycol $(CH_2OH)_2$, $\geq$ 99%) and sucrose ($C_{12}H_{22}O_{11}$, $\geq$ 99.5%) were purchased from NATCO Laboratory Chemicals Reagents. Safranin O ($\geq$ 85%, Powder), the basic dye from Sigma Aldrich, St. Louis, MO, USA (Table 1) and Ethanol ($\geq$ 99.5%) from Merck, Mumbai, India. All the reactants and solvents used were of analytical grade and were used as received. Redistilled water was employed throughout the experiments.

2.2 Preparation of graphited sand

The Graphitic sand (GS) was produced according to literatures with some modifications [29, 30]. Natural beach sand (collected from El-Minia city, Egypt) was sieved us-

Table 1. Structure and characteristics of safranin O dye.

Name	IUPAC Name	Chemical structure	Maximum wavelength	Molecular mass
Basic red 2	**3,7-dimethyl-10-phenylphenazin-10-ium-2,8-diamine;chloride**	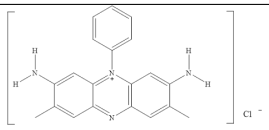	**520 nm**	**350.8 g/mol**

ing Retsch screens (Retsch, Haan, Germany) through 500 to 700 μm and natural sugar with a chemical formula of $C_{12}H_{22}O_{11}$ (as carbon source) were used to prepare GS. In a typical procedure, 100 g of sand is soaked in 100 mL 37% HCl (3 h) followed by 100 mL concentrated HNO_3 (3 h), then washed with bi-distilled water and absolute ethanol, then dried at 105 °C for 6 h. 100 g sugar dissolved in 50 mL and added to dried sand under magnetic stirring for 3 h to form a thick composite, followed by drying at 90 °C in a hot air oven to obtain sugar-coated sand. The resulting mixture was then heated under limited air at 300 °C for 2 hours to ensure the graphitization of sugar molecules. The sample was allowed to cool to room temperature to yield the black graphited sand GS.

2.3 Preparation of ZFGS

The $ZnFe_2O_4$ coated graphitic sand (ZFGS) composite was prepared by modifying a previously reported method [31, 32]. Briefly, a mixture of $ZnCl_2$ (13.6 g, 0.1 mol) and $FeCl_3.6H_2O$ (13.5 g, 0.05 mol) in a molar ratio of 2:1 (was dissolved in 50 mL ethylene glycol, and the solution was stirred for 30 minutes to obtain a homogeneous mixture. To this solution, 50 g of GS was added, and the mixture was sonicated for 10 minutes, followed by continuous magnetic stirring for 1 h to obtain thick black precipitates. The obtained precipitates were then washed with ethanol and distilled water, and finally, they were dried at 70 °C. The dried ZFGS composite was calcined for 2 h at 500 °C under a nitrogen atmosphere. Fig. 1 shows a schematic representation of the synthesis of the ZFGS composite photocatalyst.

2.4 Batch study and experimental design

In this study, the influence of four main factors was investigated using fractional factorial design SO concentration, pH, time, and photocatalyst dose. The degradation efficiency (Deg.%) of SO was considered as the dependent factor (response). Table 2 presents the four parameters and their chosen levels for the experiment. The factor levels were coded as -1 (low) and $+1$ (high). A total of eight experiments were carried out. The results were analyzed with 95% confidence intervals using the Design Expert 13.0.5.0 software. The experimental design used was a fractional factorial design containing $L^{(n-1)}$ runs, where L is the number of levels for each variant, and n is the number of operating factors. In this case, the fractional factorial design contained 8 experiments ($2^{(4-1)}$). Three replicates were performed at each of the 8 possible factorial points, resulting in a total of 24 batches of the photocatalyst being synthesized. The factorial design was carried out to identify the main effects and interactions for the degradation of SO basic dye. Table 3 exposes the design matrix of the fractional factorial design under both UV and Vis. Light. The photocatalyst ZFGS was then employed in the photocatalytic degradation of safranin O dye under both UV and visible light irradiations, resulting in a total of 48 experiments. A medium-pressure LED lamp with a power of 36 W was used as the visible light source and a medium-pressure Hg UV GL-58 lamp at a wavelength of 254 nm.

Table 2. Levels of variables and experimental range.

Variables	Unit	Code	Levels	
			Low (-1)	High (+1)
pH	-	A	4	9
Contact time	Min.	B	10	80
SO dye concentration	ppm	C	50	200
Photocatalyst Dose	**g**	**D**	**0.1**	**0.5**

2.5 Continuous photodegradation

Adsorption experiments were carried out in a continuous flow system using SO as the dye to be photodegraded by the ZFGS composite photocatalyst. The experimental setup, as depicted in Fig. 2, consisted of a 20 cm long column with an internal diameter of 1.9 cm. The photocatalyst was packed into the column at different quantities, representing various bed heights, with two layers of glass wool placed at the top and bottom of the column. Under the bottom glass wool layer, an additional layer from the glass bed was added. The

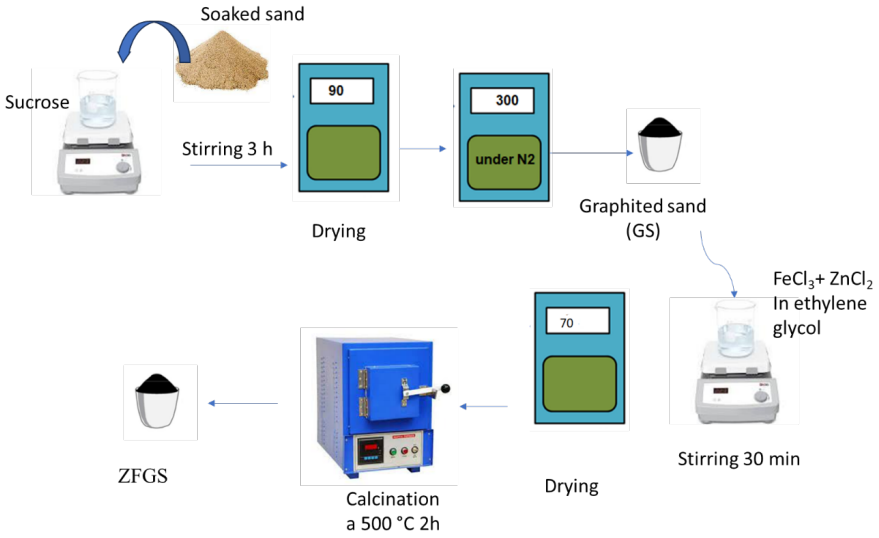

Figure 1. Schematic representation of the synthesis of ZFGS composite photocatalyst.

Table 3. Design matrix and the results of the fractional factorial design under both UV and Vis. light.

Run	pH	Dye Conc. (ppm)	Irr. Time (min)	Dose (mg)	Deg% under UV. Light		Deg% under Vis. Light	
					Actual	Predicted	Actual	Predicted
1	9	200	80	0.5	92.8	93.2	86	84.1
2	4	50	80	0.5	78.6	76.1	62	60.6
3	9	50	80	0.1	94.6	96.9	88	87.3
4	9	200	10	0.1	90.2	87.8	81	79.6
5	4	200	80	0.1	65.2	65.1	42	45.9
6	4	50	10	0.1	70.2	70.7	58	56.1
7	4	200	10	0.5	64.5	66.8	53.6	52.9
8	**9**	**50**	**10**	**0.5**	**98.8**	**98.7**	**90.4**	**94.3**

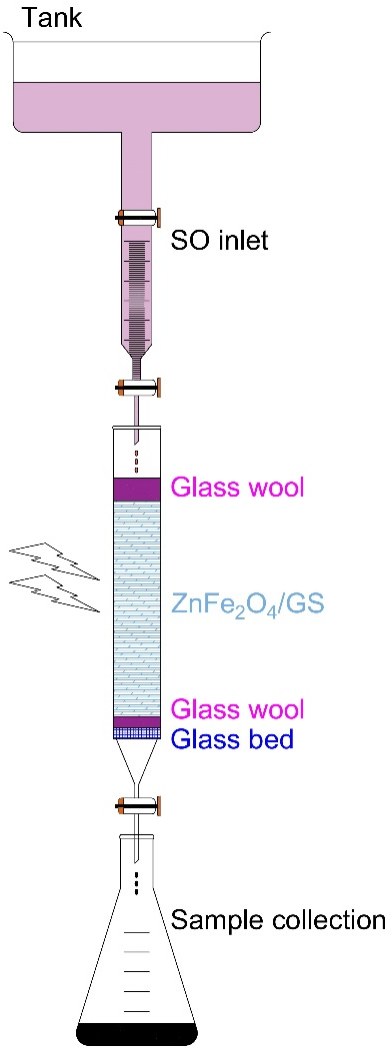

Figure 2. Schematic representation of fixed bed column.

SO dye solution of specific concentrations was fed into the column from the top in a downflow (spontaneous) manner at a fixed inflow rate, using a controlling tank filled with SO solution. Prior to each experiment, distilled water was passed through the column before the dye solutions were introduced to establish hydraulic equilibrium. The flow rate was regulated using a burette tap. The experiment was carried out in the presence of light (UV or visible). Different conditions were applied like: The initial dye concentrations ranged from 50 to 200 mg/L, the flow rate was set at 2, 4, and 8 mL/min, and the bed height was set at 2, 4, and 6 cm, and all experiments were conducted at room temperature. The percent of the dye degradation was calculated using the following equation:

$$\text{Photodegradation rate } \% = \frac{C_o - C_e}{C_o} \times 100 \qquad (1)$$

where C_o and C_e are the initial and equilibrium dye concentrations (mg/L), respectively. The concentration of the basic dye SO is determined spectrophotometrically using aUV-Vis spectrophotometer (Alpha-1502, LAXCO Inc., USA) at a maximum wavelength of 520 nm.

2.6 Photocatalyst characterization

The phase identification (XRD) was characterized using a JSX-60PA/Jeol diffractometer (Japan) equipped with a Ni-filtered CuKα radiation (λ = 1.5418 Å). The generator was operated at 35 kV and 20 mA, and the diffractometer was set with a 2θ diverging and receiving slits and a scan rate of 2 °/min. Field emission scanning electron microscopy (FE-SEM) and Energy Dispersive X-ray Spectroscopy (EDS) was performed using a FEGSEM, THERMOSCIENTIFIC QUATTRO S. Complete nitrogen adsorption/desorption isotherms at −196 °C were obtained using a NOVA 3000, version 6.10 high-speed gas sorption analyzer (Quantachrome Corporation, USA). Prior to the analysis, the sample was outgassed at 200 °C for 2 hours. From the resulting twenty-four-point adsorption and desorption isotherms, the specific surface areas (SBET) were calculated using established and widely accepted methods. Fourier-transform infrared spectroscopy (FTIR) was carried out using a Genesis-II infrared spectrometer (Mattson/U.S.A). The spectra were obtained by averaging 20 scans, with the test samples (before and after degradation) supported on KBr discs with a weight percentage of $\leq 5\%$. The frequency range was $4000 - 500$ cm^{-1}, with a resolution of 4 cm^{-1}. Zeta potential measurement of the prepared zinc ferrite was conducted using the Zetasizer Ver. 8.02 (Malvern Instruments Ltd, England). Ultraviolet-visible (UV-Vis) spectroscopy was employed to measure the optical absorption of the photocatalyst. UV–Vis diffuse reflectance spectra (DRS) of the catalysts were recorded using a Shimadzu UV 2450 spectrometer with $BaSO_4$ used as the reference material. The optical band gap of the prepared photocatalyst

was determined according to Tauc's relation [31] (Eq. (2)).

$$\alpha h\upsilon = A(h\upsilon - E_g)^{\frac{n}{2}} \quad (2)$$

the plot of $(\alpha h\upsilon)^2$ versus E is generated with $n = 1/2$ and the band gap can be determined from the slope. The energy E is calculated using Eq. (3).

$$E = h\frac{C}{\lambda} = \frac{1240}{\lambda} \quad (3)$$

where α is the absorption coefficient, Planks constant $(h) = 6.626 \times 10^{-34}$ Joule sec, υ is the frequency of light (in s^{-1}), C is the velocity of Light (2.99×10^8 meter/sec), A is the proportionality constant, E_g is the band gap, and n is a constant.

3. Results and discussion

3.1 Photocatalyst characterization

3.1.1 Morphology SEM and EDS profiles

Scanning electron microscope images (SEM) and EDS profiles for GS, ZF, and ZFGS samples are shown in Fig. 3. The grains of the sand sample exhibit a range of morphologies, including round, elongated, and irregular shapes, with lateral dimensions spanning $50-110$ nm. The SEM images further reveal the smooth surfaces of the sand grains (GS sample), with some pits and grooves present (ZFGS sample). The magnified images clearly indicated the aggregation of $ZnFe_2O_4$ over the GS. Fig. 3, show also the uniform distribution of the particles of pure zinc ferrite (ZF) which gives agreement with the XRD results in which the average particle size is in the range $70-80$ nm. Energy Dispersive X-ray Spectroscopy (EDS) analysis was performed on the prepared GS, ZF, and ZFGS samples, and the results are shown in Fig. 3. EDS provides quantitative data on elemental concentrations as shown in the tables accompanied in Fig. 3. The chemical composition of the samples was examined through point scanning, revealing the presence of all required elements. The measured compositions of Zn/Fe (0.84/0.44) agree with their theoretical ratios (2/1).

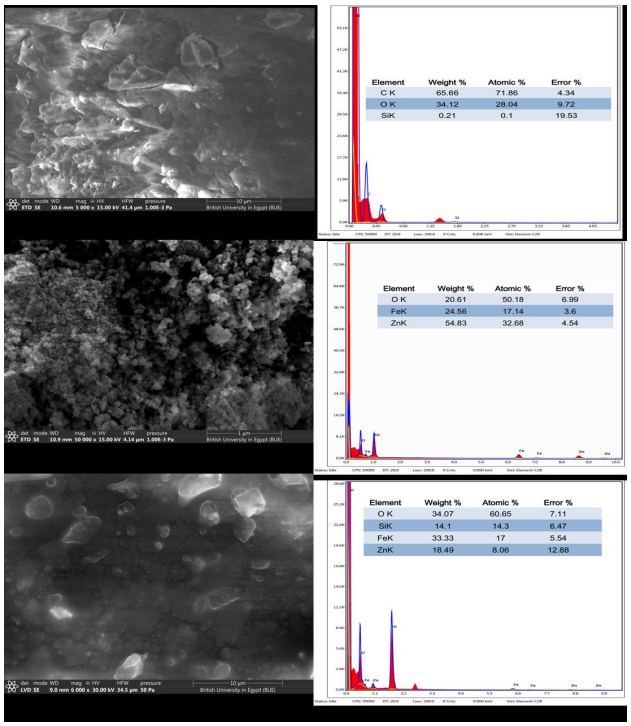

Figure 3. SEM images and EDX profile for Graphited sand, zinc ferrite, and zinc ferrite-coated graphited sand.

3.1.2 X-ray diffraction

X-ray diffraction analysis was performed to identify the phase purity and crystalline structure of the prepared photocatalysts. The XRD patterns of GS, ZF, and ZFGS composites are shown in Fig. 4. In Fig. 4, the XRD of the GS sample reveals the presence of graphite and sand components like silica, alumina, and calcium carbonate. Hexagonal and tetragonal silica are observed by the presence of diffraction peaks at $2\theta = 20.8°$, $22.15°$, $26{,}4°$ and confirmed by the presence of a diffraction peak at $2\theta = 50°$. These diffraction peaks correspond to (100), (101), (011), and (112), respectively (JCPDS N:46-1045) [30–33]. Additionally, for the graphite-coated sand composite, the strong peak at $26.6°$ and the peak at $42.9°$ are associated with the (012) and (001) plane reflections of the graphitic carbon-like structure (JCPDS No.75-2078) [30, 34, 35]. For the prepared $ZnFe_2O_4$ (ZF) sample, the characteristic diffraction peaks of $ZnFe_2O_4$ at $30.31°$, $34.62°$, $42.79°$, $53.52°$, $56.86°$, and $62.15°$ are assigned to the (220), (311), (400), (422), (511),

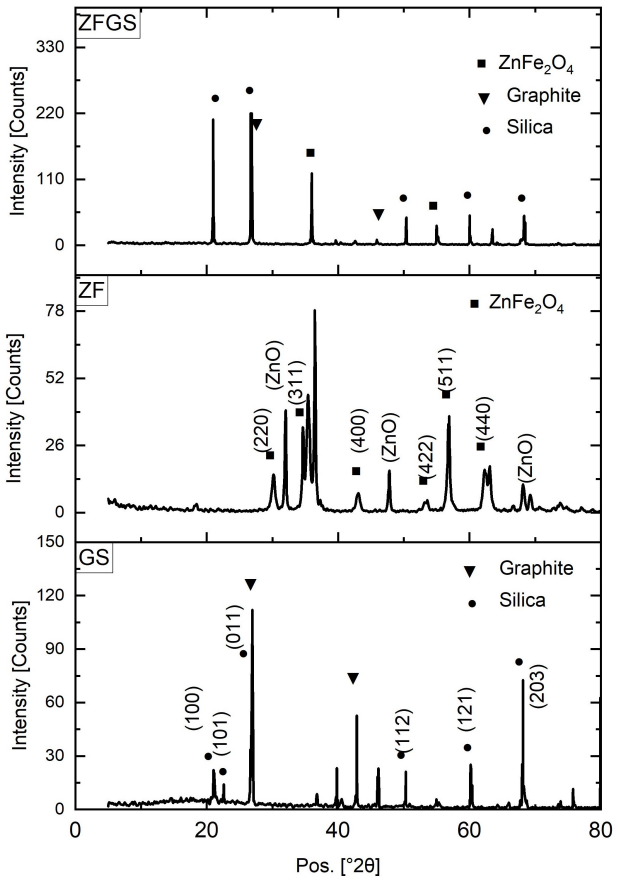

Figure 4. XRD diffractogram for Graphited sand, zinc ferrite, and zinc ferrite-coated graphited sand.

and (440) planes, respectively, as shown in Fig. 4. All these peaks correspond to the cubic phase of spinel zinc ferrite, as reported in the literature (CPDS card no.22-1012) [36]. In the case of ZFGS , the characteristic peaks of $ZnFe_2O_4$ and GS were observed in the XRD spectra. However, the intensity of the diffraction peaks in $ZnFe_2O_4$ and GS was found to decrease in the ZFGS composite. This decrease in diffraction peak intensity was ascribed to the interaction between $ZnFe_2O_4$ and GS. Using the Debye-Scherrer equation (Eq. (4)) [26], the respective sizes of ZFGS were found to be 82 nm.

$$D = \frac{K\lambda}{\beta \cos\theta} \tag{4}$$

where D is the average crystallite size (nm), K is a constant usually equal to 0.9, $\lambda = 1.54056$ Å is the wavelength of CuKα radiation, β is the full width at half-maximum (FWHM) intensity of the peak in radian, and θ is Bragg's diffraction angle.

3.1.3 FTIR spectra

The functional groups of the prepared $ZnFe_2O_4$-coated graphitic sand sample were analyzed using FTIR spectroscopy, before and after SO degradation, as depicted in Fig. 5. For the ZFGS sample before adsorption, the presence of a weak band at 1615 cm^{-1} indicates the stretching vibrations of carbonyl groups (C=O) or the bending vibrations of adsorbed water molecules (H-O-H) [33]. The presence of a sharp band at 1075 cm^{-1} was attributed to the stretching mode of the C=C bond [37], while the band at 780 cm^{-1} was assigned to Si-O stretching [38], and the band at 795 cm^{-1} confirmed the presence of quartz. The two bands at 516 and 460 cm^{-1} were assigned to M-O (M is Zn or Fe) and SiO_2 group [30]. The spectra of the sample before and after SO degradation give comparable the same bands except there are little extra bands that appear at 3730 and 2320 cm^{-1}, which are attributed to the water and carbon dioxide adsorption, respectively. Moreover, the weakening in the intensity of the bands after SO degradation indicates the interaction between the dye and the surface groups of the ZFGS photocatalysts. The FTIR spectra before and after SO degradation were largely similar, indicating that the primary functional groups of the material were retained. However, the appearance of new bands at 3730 cm^{-1}, attributed to water adsorption, and 2320 cm^{-1}, associated with carbon dioxide adsorption, suggests the adsorption of degradation byproducts on the photocatalyst surface. Additionally, the weakening of band intensities after SO degradation indicates significant interactions between the SO dye and the surface functional groups of the ZFGS, likely resulting from the photocatalytic degradation process.

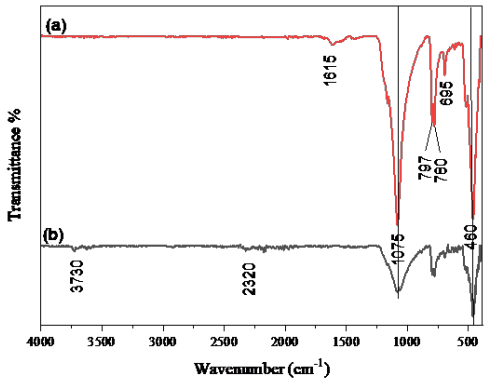

Figure 5. FTIR spectra for ZFGS before (a) and after (b) safranin o photocatalysis.

3.1.4 Surface texture (BET method)

Fig. 6(a) shows the N_2 adsorption/desorption isotherm and pore size distribution of the photocatalysts. The isotherms exhibited a type IV pattern according to IUPAC classifi-

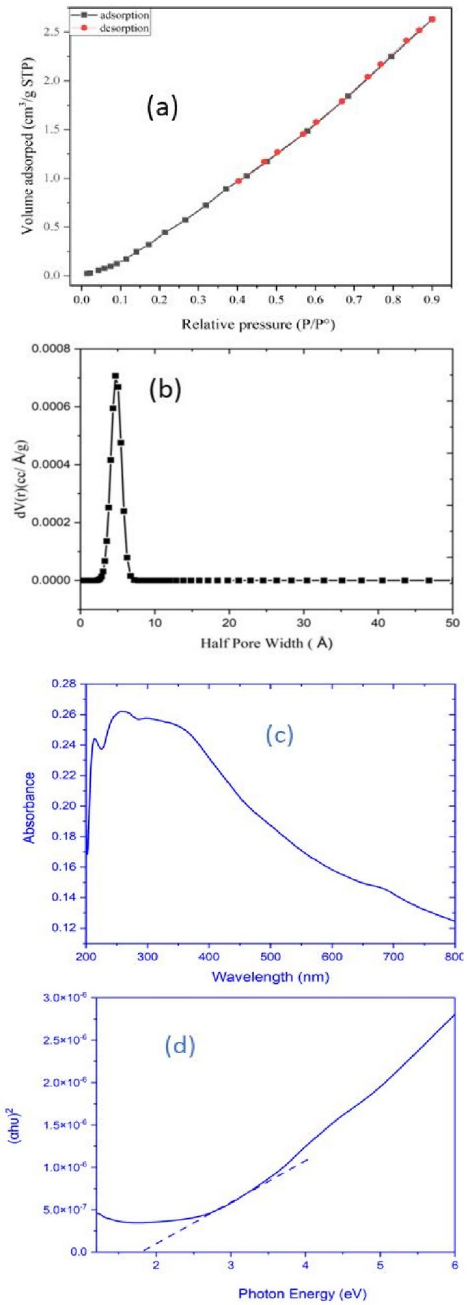

Figure 6. (a) N_2 sorption isotherm, (b) pore size distribution, (c) The absorption spectra obtained in the DRS technique, and (d) Band gap calculation for ZFGS

Table 4. Surface properties, crystallite size, zeta potential, and band gap for ZFGS catalyst.

C_{BET}	S_{BET} m^2/g	Total pore volume (cm^3/g)	Mean pore diameter (nm)	Crystallite size (nm)*	Zeta potential (mV)	Band Gap (eV)
0.99	6.7	0.0041	2.58	82	-14	1.77

*From Debye-Scherrer equation (Eq. (4))

cations, indicating the mesoporous nature of the prepared sample. The pore size distribution data (Fig. 6b) revealed that most pores are smaller than 20 nm (micropores). The BET-specific surface area of ZFGS is found to be 6.7 m^2/g. Table 4 shows the textural data of the prepared sample.

3.1.5 Zeta potential and DRS

The zeta potential is a measure of the electrical charge at the slipping plane surrounding a particle. The zeta potential of the prepared sample powder was measured by Malvern zetasizer and found to be -14 mV, indicating that the particles have a negative surface charge, which leads to repulsive forces between the particles and enhancing the stability of the colloidal system. The magnitude of the zeta potential (-14 mV in this case) suggests the strength of the repulsive or attractive forces between the particles. The negative surface charge can influence the adsorption behavior of the particles, making them more likely to adsorb positively charged species. Fig. 6(c) presents the absorption spectra obtained in the DRS technique of the prepared catalysts, showing that the main absorption peak occurs in the UV region at approximately 335 nm. According to Eq. (2), the plot of $(\alpha h\upsilon)^2$ versus E is generated with $n = 1/2$ and exposed in Fig. 6(d). The band gap can be determined from the slope of Fig. 6(d) and found to be 1.77 eV, which is in agreement with previous data [39, 40]. The band gap energy of less than 2 eV corresponds to light absorption at wavelengths up to approximately 620 nm, which is well within the visible spectrum ($400-700$ nm). This explains the material's capability to harness visible light for photocatalytic activity. The band gap energy, a crucial optical property of semiconductors representing electronic transitions between the valence and conduction bands, can be estimated using absorption edge wavelengths and analyzed through Kubelka-Munk and Tauc plots. Diffuse reflectance spectroscopy (DRS) provides valuable insights into macroscopic optical properties, including reflectance, absorption, and dispersion, which are influenced by photon re-emission, particle size distribution, and material structure [41].

3.2 Photocatalytic studies of SO basic dye

3.2.1 Batch adsorption study and experimental design

The accuracy and validity of the fitted statistical model were evaluated through a series of statistical analyses. These include normal plots, Pareto charts, residual analysis, Contour plots, 3D surface, predicted vs actual, and ANOVA). Fig. 7 illustrates factorial design plots of Deg.% for both photodegradation processes under UV and visible lights. The impact of various factors and their interactions on the photodegradation process can be analyzed using different methods. The normal plot provides a more accurate assessment of the significant influence exerted by different factors and interactions. In the normal plot of standardized effects shown in Fig. 7, factors that are near to the line indicate insignificant influence on the degradation process, while those that are far from the line indicate significant effects. For both processes, the pH is the most significant factor. The Pareto diagram allows for a comparison of absolute values thus according to the Pareto chart, factors on the higher side of the line positively influence the SO degradation, while those on the lower side of the line have a negative impact or are non-significant for the sorption process. The graphs comparing predicted and actual values (Fig. 7) show data points that are close to a straight line, indicating the suitability of the model, as supported by Eqs. (5) and (6) and Table 3.

$$\text{Deg.}\% = 52.27 + 4.90 * \text{pH} - 0.05 * \text{dye conc.} + 0.03 * \text{Irr.Time} + 9.06 * \text{Dose} \quad (5)$$

$$\text{Deg.}\% = 31.89 + 6.49 * \text{pH} - 0.06 * \text{dye conc.} - 0.02 * \text{Irr.Time} + 14.37 * \text{Dose} \quad (6)$$

Based on the analysis of variance (ANOVA) test results presented in Table 5 and 6. The Model F-values are 42.1 and 41.2 for two processes under UV and vis. Light, respectively, implies the models are significant. The p-values are found to be less than 0.05 imply that the models are statistically significant. The predicted R-squared values are in reasonable agreement with the adjusted R-squared

Table 5. ANOVA for selected factorial model under UV light.

Source	Sum of Squares	df	Mean Square	F-value	p-value	
Model	1340.14	4	335.04	42.10	0.0057	significant
A-pH	1198.05	1	1198.05	150.55	0.0012	
B-Dye Conc.	108.78	1	108.78	13.67	0.0343	
C-Irr. Time	7.03	1	7.03	0.8836	0.4166	
D-Dose	26.28	1	26.28	3.30	0.1668	
Residual	23.87	3	7.96			
Cor Total	1364.02	7				

Std. Dev 2.82; R^2 0.983; Adjusted R^2 0.96; Predicted R^2 0.88; Adeq Precision 15.06, and C.V.% 3.45

Table 6. ANOVA for a selected factorial model under Vis. light.

Source	Sum of Squares	df	Mean Square	F-value	p-value	
Model	2335.46	4	583.87	41.18	0.0059	significant
A-pH	2106.00	1	2106.00	148.54	0.0012	
B-Dye Conc.	160.21	1	160.21	11.30	0.0437	
C-Irr. Time	3.13	1	3.13	0.2204	0.6707	
D-Dose	66.13	1	66.13	4.66	0.1196	
Residual	42.54	3	14.18			
Cor Total	2377.99	7				

Std. Dev 3.77; R^2 0.98; Adjusted R^2 0.96; Predicted R^2 0.87; Adeq Precision 16.3, and C.V.% 5.37

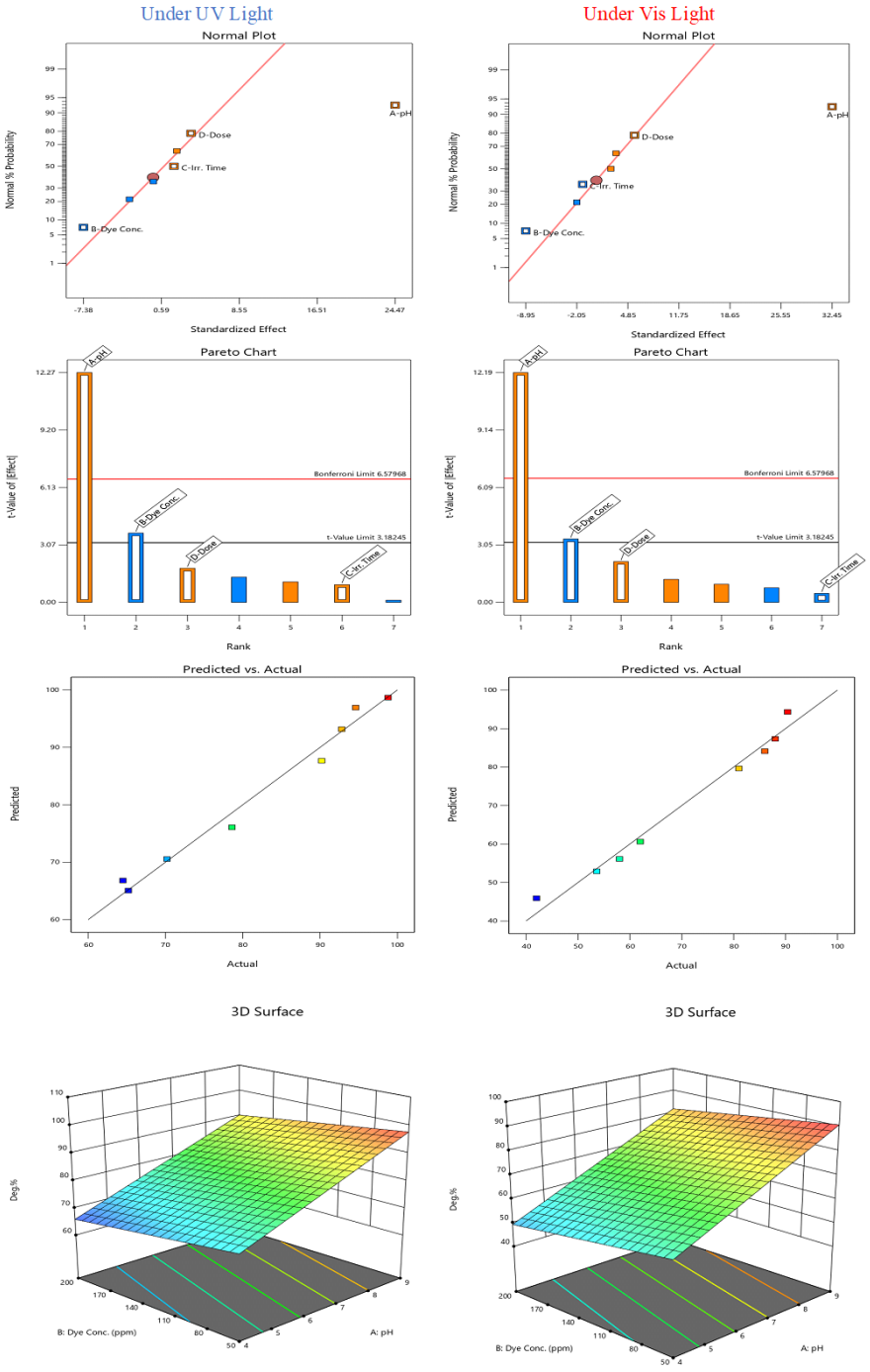

Figure 7. Fractional factorial plots for ZFGS under UV and Vis. light.

values for the two processes, with the difference being less than 0.2. Adequate precision measures the signal-to-noise ratio, and a ratio greater than 4 is considered desirable [26]. The coefficients of variation (C.V.%) are 3.45% and 5.37% for the two photodegradation processes under UV and Vis. Light, respectively, indicating that the deviations between the actual and predicted values are low. This confirms the precision and reliability of the experiments.

The optimal conditions for the photodegradation of the dye SO under both UV and visible light were found to be the same, based on the 3D surface plots (Fig. 7). These optimal conditions were pH: 9, dye concentration: 50 mg/L, reaction time: 45 minutes, and catalyst dose: 0.3 g. Under these conditions, photodegradation is achieved approximately 99% under UV light and around 90% under visible light.

3.2.2 Fixed bed continuous photodegradation

The fixed bed continuous approach provides valuable insights into the dynamic behavior, mass transfer, and kinetics of photocatalysis processes, which is crucial for the design and scale-up of industrial-scale systems. The concentration of the target compound in the effluent is monitored over time, generating a breakthrough curve. The breakthrough curve provides information on the photocatalysis capacity, mass transfer zone, and the optimal operating time before regeneration is required. Due to the overall results of batch studies under UV and Vis. Ligh give comparable Deg.%, the fixed bed studies only conducted under visible light. In his study, the change in flow rate (2, 4, and 8 mL/min), dye concentration (50, 100, and 200 mg/L), and the height of the column bed (2, 4, and 6 cm) were studied under Vis. irradiation.

i) Flow-rate effect

The effect of the inlet flow rate of the SO-polluted water sample on the photodegradation was investigated using a fixed-bed column packed with ZFGS (under Vis. light). The study was conducted with various feed flow rates of 2, 4, and 8 mL/min, while maintaining a fixed bed height of 4 cm (with a particle size of $0.5-0.7$ mm) and an inlet SO concentration of 100 mg/L. Fig. 8(a) illustrates the breakthrough curves of the SO degradation at the three different flow rates investigated. The analysis results corresponding to these breakthrough curves are presented in Table 6. From Fig. 8(a), increasing the flow rate led to shorter breakthrough times and steeper breakthrough curves, indicating the insufficient residence time template in the column [42]. The increased flow rate also positively influenced the total amount of SO degraded (mg). On the other hand, the slowest breakthrough curve was observed at the lowest flow rate of 2 mL/min. The highest dye degradation efficiency of 88% was recorded at the flow rate of 2 mL/min. As the inlet flow rate increased from 2 to 8 mL/min, the degradation percent of the prepared photocatalyst changed from 88% to 78%. These results suggest that the flow rate has a significant impact on the photodegradation performance of the ZFGS

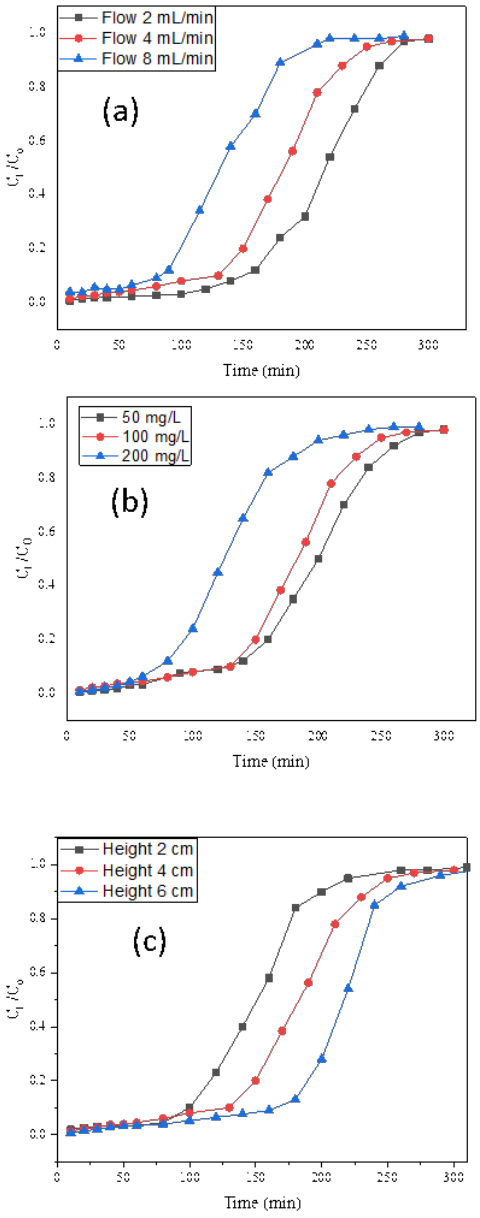

Figure 8. Experimental breakthrough curves for SO photodegradation (a) at different flowrates (constant bed height 4 cm, and initial dye concentration 100 mL/L), (b) at different initial dye concentrations (constant bed height 4 cm, and flowrate 4 mL/min) and (c) at different bed heights (constant initial dye concentrations 100 mg/L, and flowrate 4 mL/min).

photocatalyst, with lower flow rates leading to higher dye photodegradation efficiencies and bed capacities [43].

ii) Dye concentration effect

The study investigated the impact of the SO dye concentration on the photodegradation process. Various initial inlet SO concentrations ranging from 50 to 200 mg/L were examined while maintaining the same flow rate of 4 mL/min and bed height of 4 cm. The initial SO concentration had a significant influence on the photodegradation capacity, as illustrated in Fig. 8(b) and Table 6. The photodegradation amount of SO dye increased from 53.8 to 123 mg as the initial feed concentration of SO

Table 7. The breakthrough calculations.

Flowrate (mL/min)	C_o (mg/L)	Height (cm)	t_e (min)	Effluent Volume (mL)	m_{total}[a] (mg)	C_e (mg/L)	Deg.%	m_D[b]
2	100	4	280	560	56	12	88	49.3
4	100	4	250	1000	100	15.4	84.6	84.6
8	100	4	210	1680	168	22	78	131
4	50	4	280	1120	56	2	96	53.8
4	200	4	200	800	160	46	77	123
4	100	2	220	880	88	18.6	81.4	71.6
4	100	6	300	1200	120	3.5	96.5	116

[a]total mass of dye delivered to column (mg)=flowrate*Co*t/1000;
[b]total mass degraded = Deg% *m_{total}

was raised from 50 to 200 mg/L, respectively. This result demonstrates that the change in concentration gradient can affect the saturation rate, the breakthrough time, and the diffusion process. The SO loading rate increased with increasing the feed concentration, due to a decrease in the mass-transfer driving force for a fixed sorption bed length. Additionally, a higher feed concentration of the dye provides a greater concentration gradient for the mass-transfer process, resulting in a higher amount of dye being degraded from the solution and an increased breakthrough time. Moreover, a higher concentration gradient leads to an increase in the diffusion coefficient, which facilitates faster transport of dye from the solution on the beds and an earlier breakthrough time. Therefore, higher column performance can be achieved with higher initial concentrations in the solution, these results well agree with reported data [42, 43].

iii) Bed height effect

Fig. 8(c) displays the breakthrough profiles for SO degradation over zinc ferrite graphited sand composite at three bed heights: 2, 4, and 6 cm, with a constant flow rate of 4 mL/min and an inlet SO concentration of 100 mg/L. As indicated in Table 7, the breakthrough time increased with greater bed height. A similar pattern was observed for exhaustion time. At higher bed heights, the mass transfer zone took longer to reach the end of the column, resulting in extended breakthrough and exhaustion times. Furthermore, increasing the photocatalytic mass (bed height) provided a larger service area, enhancing the volume of treated solution [44]. The increase in height from 2 to 6 cm had a significant effect on the degradation percent (increased from 81.4% to 96.5) and the amount of degraded dye increased from 71.6 to 116 mg.

3.3 Reusability performance

Reusability is an essential criterion for evaluating the performance of the photocatalysts and their practicality for industrial applications, as it can significantly reduce operational costs and enhance the process's economic viability. After the initial fixed bed column photocatalysis process, the photocatalyst (ZFGS) recovered by centrifugation, washing with water and ethanol, followed by drying under vacuum for 6 hours. The catalyst's reusability was tested over six cycles under optimal conditions (25 °C, Flowrate 4 mL/min, bed height 4 cm, Co 100 mg/L, and total effluent volume 1000 mL). As shown in Table 8, the 1st cycle exposes about 94% degradation. The recycled catalyst experienced only slight deactivation after four cycles to become 76.4% for the fifth cycle. This deactivation of the performance is possibly due to gradual pore blockage.

Table 8. Reusability of ZFGS photocatalyst for SO degradation (25 °C, Flowrate 4 mL/min, bed height 4 cm, Co 100 mg/L, and total effluent volume 1000 mL).

Cycle	1	2	3	4	5	6
Degradation %	94.2	92.8	90.4	88	76.4	71.8

3.4 Photocatalytic mechanism

Based on the previous literature [45–49], Fig. 9 and Eq. (7-12) illustrate a suggested mechanism for SO photocatalytic degradation over $ZnFe_2O_4$ nanoparticles. Upon irradiation by a UV or Vis. lamp, electrons in the valence band (VB) of $ZnFe_2O_4$ are excited to the conduction band (CB), forming number of holes in the VB. The photoinduced holes can either directly degrade the SO dye or interact with surface-bound H_2O or OH^- to generate hydroxyl radicals (·OH), which are highly oxidizing agent. The excited electrons tend to pair with adsorbed oxygen molecules, resulting in the formation of strong hydroxyl radicals. These radicals then degrade the SO dye.

$$ZnFe_2O_4 + h\upsilon \rightarrow e^-_{(CB)} + h^+_{(VB)} \quad (7)$$

$$h^+_{VB} + H_2O \rightarrow {}^{\cdot}OH + H^+ \quad (8)$$

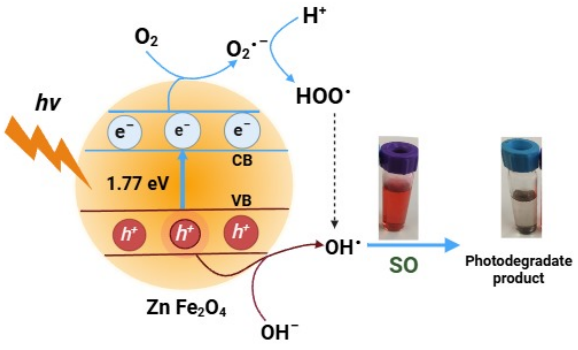

Figure 9. Schematic illustration of photocatalytic mechanism.

Table 9. Photocatalytic degradation of SO dye over different composites.

Photocatalyst	Photolight	Removal %	Ref.
TiO_2	UV-254 nm	60	[1]
Ag–TiO_2	UV-254 nm	96	[1]
PUCP1@rGO	Vis. Light	76	[50]
$LaNiSbWO_4$-G-PANI	Vis. light (>420 nm)	84	[51]
CuSNPS	UV irradiation	95	[52]
Titania coated silica	UV light	93.3	[**?**]
ZnS nanoparticles	UV–vis	51	[**?**]
NiO-MgO	Vis. Light	98.4	[53]
biosynthesized ZnO	solar irradiation	96.9	[54]
ZnO	UV light (254 nm)	87	[55]
$ZnFe_2O_4$ coated GS	Vis. Light	90.4	This study
$ZnFe_2O_4$ coated GS	UV- (254 nm)	98.8	This study

$$h^{+}_{(VB)} + OH^{-} \rightarrow {}^{\cdot}OH \quad (9)$$

$$e^{-}_{(CB)} + O_2 \rightarrow O_2^{\cdot -} \quad (10)$$

$$O_2^{\cdot -} + H^{+} \rightarrow HO_2^{\cdot} \quad (11)$$

$$H^{+} + HO_2^{\cdot} + 2e^{-}_{(CB)} \rightarrow OH^{-} + OH^{\cdot} \quad (12)$$

3.5 Comparison with other studies

For comparing different photocatalysts used in SO photocatalytic degradation, key parameters to consider include their synthesis method, activation light range (UV or visible), and degradation efficiency. Below is an example of a comparative table for such photocatalysts: Table 9 exposes the different photocatalysts used for SO degradation. $ZnFe_2O_4$/GS stands out for its dual UV-visible light activation and adaptability to continuous systems, making it more practical for large-scale SO degradation. Traditional TiO_2 offers excellent efficiency under UV light but is limited to batch systems and sensitive to specific operational conditions. Recent materials like PUCP1@rGO provide visible light activation but may have moderate efficiency or operational restrictions.

4. Conclusions

Photocatalysis has proven to be an effective approach for water treatment, leveraging light to degrade pollutants. In this study, a zinc ferrite-coated graphitic sand ($ZnFe_2O_4$/GS) photocatalyst was successfully synthesized using the coprecipitation method and applied for the photodegradation of safranin O dye under various conditions. The structural integrity and composition of the $ZnFe_2O_4$/GS catalyst were confirmed by XRD analysis, while its negative zeta potential facilitated efficient interaction with the dye molecules. Both batch and continuous photocatalytic strategies were employed, with a fractional factorial design used to evaluate the effects of key variables, including pH, dye concentration, irradiation time, and catalyst dosage. ANOVA results revealed that pH had the most significant impact on the degradation process, and higher degradation efficiencies were achieved under UV light compared to visible light. The optimization process validated the model with a high correlation coefficient ($R^2 > 0.98$) and a significant F-ratio. Optimal degradation efficiencies of 98.8% under UV light and 90.4% under visible light were achieved at pH 9, 50 mg/L dye concentration, 0.3 g catalyst dosage, and 45 minutes of irradiation time. Continuous photodegradation experiments using a fixed-bed column confirmed the effectiveness of $ZnFe_2O_4$/GS, demonstrating favorable mass transfer properties and extended breakthrough times. The $ZnFe_2O_4$/GS photocatalyst demonstrated strong reusability, maintaining high degradation efficiency (94% in the 1st cycle) with only slight deactivation after six cycles, making it a cost-effective and practical option for industrial wastewater treatment. These findings highlight the potential of $ZnFe_2O_4$/GS as a cost-effective and efficient photocatalyst for environmental remediation, offering a promising solution for the sustainable treatment of toxic pollutants in water systems. A cost-effective and scalable $ZnFe_2O_4$/GS photocatalyst was synthesized via a simple coprecipitation method, offering a practical solution for large-scale applications. The photocatalyst effectively utilizes both UV and visible light, enhancing its versatility and potential for real-world applications. The study demonstrates the viability of $ZnFe_2O_4$/GS in a fixed-bed continuous system, advancing beyond laboratory-scale batch processes.

Authors contributions

Ms. Essam; investigation, data analysis and article draft writing. Dr. Matter; data extraction, methodology, and article writing. Dr. Esmail; literature quality evaluation, meta-analysis, and writing – review, and editing. Ass. Prof. Khalaf; research director, objection discussion and ruling. All authors agree with the final version of the article and the author list. All authors read and approved the final manuscript.

Availability of data and materials

The datasets generated and analyzed during the current study are available from Hussein A. Khalaf.

Conflict of interests

The author declares that they have no known competing financial interests or personal relationships that could have appeared to influence the work reported in this paper.

References

[1] M. El-Kemary, Y. Abdel-Moneam, M. Madkour, and I. El-Mehasseb. *J. Lumin*, **131(4)**(2011):570–576. DOI: https://doi.org/10.1016/j.jlumin.2010.10.025.

[2] A. I. Rehan, A. I. Rasee, M. E. Awual, R. Waliullah, M. S. Hossain, K. T. Kubra, M. S. Salman, M. M. Hasan, M. N. Hasan, and M. C. Sheikh. *Colloids Surf., A*, **673**(2023):131859. DOI: https://doi.org/10.1016/j.colsurfa.2023.131859.

[3] M. M. Hasan, M. S. Salman, M. N. Hasan, A. I. Rehan, M. E. Awual, A. I. Rasee, R. Waliullah, M. S. Hossain, K. T. Kubra, and M. C. Sheikh. *Colloids Surf., A*, **673**(2023):131794, . DOI: https://doi.org/10.1016/j.colsurfa.2023.131794.

[4] K. Castro and R. Abejón. *Membranes*, **14**(2024):180. DOI: https://doi.org/10.3390/membranes14080180.

[5] M. Sgroi, S. A. Snyder, and P. Roccaro. *Chemosphere*, **273**(2021): 128527. DOI: https://doi.org/10.1016/j.chemosphere.2020.128527.

[6] D. Ma, H. Yi, C. Lai, X. Liu, X. Huo, Z. An, L. Li, Y. Fu, B. Li, and M. Zhang. *Chemosphere*, **275**(2021):130104. DOI: https://doi.org/10.1016/j.chemosphere.2021.130104.

[7] R. Waliullah, A. I. Rehan, M. E. Awual, A. I. Rasee, M. C. Sheikh, M. S. Salman, M. S. Hossain, M. M. Hasan, K. T. Kubra, and M. N. Hasan. *J. Mol. Liq*, **388**(2023):122763. DOI: https://doi.org/10.1016/j.molliq.2023.122763.

[8] H. Zangeneh, A. A. L. Zinatizadeh, M. Habibi, M. Akia, and M. Hasnain Isa. *J. Ind. Eng. Chem.*, **26**(2015):1–36. DOI: https://doi.org/10.1016/j.jiec.2014.10.043.

[9] J. A. Garrido-Cardenas, B. Esteban-García, A. Agüera, J. A. Sánchez-Pérez, and F. Manzano-Agugliaro. *Int. J. Environ. Res. Public Health*, **17(1)**(2020):170. DOI: https://doi.org/10.3390/ijerph17010170.

[10] X. Huo, Y. Yang, Q. Niu, Y. Zhu, G. Zeng, C. Lai, H. Yi, M. Li, Z. An, D. Huang, Y. Fu, B. Li, L. Li, and M. Zhang. *Chem. Eng. J.*, **403**(2021):126363. DOI: https://doi.org/10.1016/j.cej.2020.126363.

[11] H. A. Khalaf and R. F. A. El-Baki. *Iranian Journal of Catalysis*, **13(3)**(2023):285–297. DOI: https://doi.org/10.30495/ijc.2023.1985433.2006.

[12] A. Yousefi and A. Nezamzadeh-Ejhieh. *Iran. J. Catal.*, **11(3)**(2021): 247–259. URL https://oiccpress.com/ijc/article/view/3600.

[13] M. Rezaei, A. Nezamzadeh-Ejhieh, and A. R. Massah. *Ecotoxicol. Environ. Saf.*, **269**(2024):115927. DOI: https://doi.org/10.1016/j.ecoenv.2024.115927.

[14] D. K. L. Harijan, S. Gupta, S. K. Ben, and A. Srivastava. *J. Singh, and V. Chandra, Physica B*, **627**(2022):413567. DOI: https://doi.org/10.1016/j.physb.2021.413567.

[15] K. M. Lee, C. W. Lai, K. S. Ngai, and J. C. Juan. *Water Res.*, **88**(2016):428–448. DOI: https://doi.org/10.1016/j.watres.2015.09.045.

[16] H. Liu, C. Han, C. Shao, S. Yang, K. Li, B. Li, K. Li, J. Ma, and Y. Liu. *ACS App. Nano Mater.*, **2(8)**(2019):4879–4890. DOI: https://doi.org/10.1021/acsanm.9b00838.

[17] I. Hasan, C. Shekhar, I. I. Bin Sharfan, R. A. Khan, and A. Alsalme. *ACS Omega*, **5(49)**(2020):32011–32022, . DOI: https://doi.org/10.1021/acsomega.0c04917.

[18] A. Islam, S. H. Teo, M. T. Islam, A. H. Mondal, H. Mahmud, S. Ahmed, M. Ibrahim, Y. H. Taufiq-Yap, G. Abdulkareem-Alsultan, and M. L. Hossain. *Renewable Sustainable Energy Rev.*, **208**(2025): 115033, . DOI: https://doi.org/10.1016/j.rser.2024.115033.

[19] A. Islam, T. Islam, H. Mahmud, O. Raihan, M. S. Islam, H. M. Marwani, M. M. Rahman, A. M. Asiri, M. M. Hasan, and M. N. Hasan. *Int. J. Hydrogen Energy*, **67**(2024):458–486, . DOI: https://doi.org/10.1016/j.ijhydene.2024.04.142.

[20] Z. O. Basyigit and Z. Ciğeroğlu. *Fibers and Polym.*, **25(8)**(2024): 2913–2923. DOI: https://doi.org/10.1007/s12221-024-00642-0.

[21] Z. Ciğeroğlu and Z. Omerogullari Basyigit. *J. Mol. Liq.*, **412**(2024): 125895. DOI: https://doi.org/10.1016/j.molliq.2024.125895.

[22] B. Erim, Z. Ciğeroğlu, S. Şahin, and Y. Vasseghian. *Chemosphere*, **291**(2022):132929. DOI: https://doi.org/10.1016/j.chemosphere.2021.132929.

[23] V. Vaiano, O. Sacco, D. Pisano, D. Sannino, and P. Ciambelli. *Chem. Eng. Sci.*, **137**(2015):152–160. DOI: https://doi.org/10.1016/j.ces.2015.06.023.

[24] A. Sraw, T. Kaur, I. Thakur, A. Verma, R. K. Wanchoo, and A. P. Toor. *J. Mol. Struct.*, **1265**(2022):133392. DOI: https://doi.org/10.1016/j.molstruc.2022.133392.

[25] A. R. Soleymani, A. M. Tavassoli, and H. Rezaei-Vahidian. *Chem. Eng. Res. Des.*, **190**(2023):759–776. DOI: https://doi.org/10.1016/j.cherd.2022.12.047.

[26] A. M. Kosba, G. M. El-Naggar, E. Elmaghraby, and H. A. Khalaf. *Catal. Surv. Asia*, (2024):1–20. DOI: https://doi.org/10.1007/s10563-024-09429-y.

[27] S. Saensook and A. Sirisuk. *J. Water Process Eng.*, **45**(2022): 102495. DOI: https://doi.org/10.1016/j.jwpe.2021.102495.

[28] A. W. Skinner, A. M. DiBernardo, A. M. Masud, N. Aich, and A. H. Pinto. *J. Environ. Chem. Eng.*, **8(5)**(2020):104235. DOI: https://doi.org/10.1016/j.jece.2020.104235.

[29] S. S. Gupta, T. S. Sreeprasad, S. M. Maliyekkal, S. K. Das, and T. Pradeep. *ACS Appl. Mater. Interfaces*, **4(8)**(2012):4156–4163. DOI: https://doi.org/10.1021/am300889u.

[30] S. Gautam, P. Shandilya, B. Priya, V. P. Singh, P. Raizada, R. Rai, M. Valente, and P. Singh. *Sep. Purif. Technol.*, **172**(2017):498–511. DOI: https://doi.org/10.1016/j.seppur.2016.09.006.

[31] M. Cobos, P. de la Presa, I. Llorente, A. García-Escorial, A. Hernando, and J. A. Jiménez. *J. Alloys Compd.*, **849**(2020):156353. DOI: https://doi.org/10.1016/j.jallcom.2020.156353.

[32] B. Jyothish and J. Jacob. *J. Alloys Compd.*, **863**(2021):158352. DOI: https://doi.org/10.1016/j.jallcom.2020.158352.

[33] N. Meftah and M. S. Mahboub. *Silicon*, **12(1)**(2020):147–153. DOI: https://doi.org/10.1007/s12633-019-00109-5.

[34] A. Shalaby, D. Nihtianova, P. Markov, A. Staneva, R. Iordanova, and Y. Dimitriev. *Bulg. Chem. Commun.*, **47(1)**(2015):291–295.

[35] M. J. McAllister, J. L. Li, D. H. Adamson, H. C. Schniepp, A. A. Abdala, J. Liu, M. Herrera-Alonso, D. L. Milius, R. Car, R. K. Prud'homme, and I. A. Aksay. *Chem. Mater.*, **19(18)**(2007):4396–4404. DOI: https://doi.org/10.1021/cm0630800.

[36] L. L. T. Nguyen, K. D. M. Nguyen, T. A. Nguyen, and K. No. *Ceram. Int.*, **48(3)**(2022):4090–4095. DOI: https://doi.org/10.1016/j.ceramint.2021.10.199.

[37] J. Wu, S. Bai, X. Shen, and L. Jiang. *Appl. Surf. Sci.*, **257(3)**(2010): 747–751. DOI: https://doi.org/10.1016/j.apsusc.2010.07.058.

[38] P. Sathya, G. Velraj, and S. Meyvel. *Adv Appl. Sci. Res.*, **3(2)**(2012): 776–779.

[39] S. S. Jadhav, V. Y. Salunke, C. H. Jadhav, S. H. Mujawar, and S. R. Bhongale. *Macromolecular Symposia*, (2021).
DOI: https://doi.org/10.1002/masy.202100070.

[40] G. Joshi, N. Saxena, R. Mangal, A. Mishra, and T. Sharma. *Bull. Mater. Sci.*, **26**(2003):387–389.
DOI: https://doi.org/10.1007/BF02711181.

[41] M. Farsi and A. Nezamzadeh-Ejhieh. *Surf. Interfaces*, **32**(2022): 102148.
DOI: https://doi.org/10.1016/j.surfin.2022.102148.

[42] N. Fallah and M. Taghizadeh. *J. Environ. Chem. Eng.*, **8(5)**(2020): 104079.

[43] H. A. Khalaf. *Sep. Sci. Technol.*, **49(4)**(2014):523–532.
DOI: https://doi.org/10.1080/01496395.2013.853084.

[44] T. Claes, T. Van Gerven, and M. Leblebici. *Chem. Eng. J.*, **403**(2021): 126355.
DOI: https://doi.org/10.1016/j.cej.2020.126355.

[45] J. Zhu, Y. Zhu, Z. Chen, S. Wu, X. Fang, and Y. Yao. *Int. J. Environ. Res. Public. Health.*, **19(17)**(2022):10710.
DOI: https://doi.org/10.3390/ijerph191710710.

[46] F. Ajormal, F. Moradnia, S. Taghavi Fardood, and A. Ramazani. *J. Chem. Rev.*, **2(2)**(2020):90–102.

[47] D. Chahar, S. Taneja, S. Bisht, S. Kesarwani, P. Thakur, A. Thakur, and P. Sharma. *J. Alloys Compd.*, **851**(2021):156878.
DOI: https://doi.org/10.1016/j.jallcom.2020.156878.

[48] S. Ghattavi and A. Nezamzadeh-Ejhieh. *Desalin. Water Treat.*, **166**(2019):92–104.
DOI: https://doi.org/10.5004/dwt.2019.24638.

[49] S. A. Mirsalari, A. Nezamzadeh-Ejhieh, and A. R. Massah. *Spectrochim. Acta, Part A*, **288**(2023):122139.
DOI: https://doi.org/10.1016/j.saa.2022.122139.

[50] K. Arya, A. Kumar, A. Sharma, S. Singh, S. K. Sharma, S. K. Mehta, and R. Kataria. *Top. Catal.*, **65(19)**(2022):1924–1937.
DOI: https://doi.org/10.1007/s11244-022-01701-7.

[51] W. C. Oh, K. N. Fatema, Y. Liu, C. S. Lim, K. Y. Cho, C. H. Jung, and M. R. U. D. Biswas. *J. Photochem. Photobiol., A*, **394**(2020): 112484.
DOI: https://doi.org/10.1016/j.jphotochem.2020.112484.

[52] M. F. El-Berry, S. A. Sadeek, A. M. Abdalla, and M. Y. Nassar. *Mater. Res. Bull.*, **133**(2021):111048.
DOI: https://doi.org/10.1016/j.materresbull.2020.111048.

[53] N. YAHI, L. AOUDJIT, I. KAHINA, I. BAALACHE, and D. SELLAM. *Cellul. Chem. Technol.*, **58**(2024).

[54] Mandal G. and B. Bhattacharjee. *The Scientific Temper.*, **15(02)**(2024):2092–2098.
DOI: https://doi.org/10.58414/SCIENTIFICTEMPER.2024.15.2.19.

[55] M. V. Kangralkar, J. Manjanna, N. Momin, K. Rane, G. Nayaka, and V. A. Kangralkar. *Environ. Nanotechnol. Monit. Manage.*, **16**(2021): 100508.
DOI: https://doi.org/10.1016/j.enmm.2021.100508.